

The long and short of it



Jordan Peckham



Siu O'Young



John T. Jacobs

Peckham, O'Young, and Jacobs discuss the ins and outs of infrared imaging for ocean based sensing.

Who should read this paper?

Anyone interested in the theory and science of infrared imaging, as well as those interested in the application of thermal imaging as a means to remotely study and map oceanographic characteristics and to monitor human activity and wildlife in our oceans.

Why is it important?

Any and every technology that advances our ability to study and further understand the ocean, its complexities, and the life it supports represents another step forward in our knowledge of our surrounding environment. The technology and application of medium and long wave infrared imaging is relatively mature from a terrestrial perspective, applied in areas ranging from medicine, agriculture, and fire detection. The application of such technology continues to advance from an ocean perspective; however, the subtleties of a dynamic ocean environment contribute to a complex scenario. That said, ongoing advances in such areas as ocean temperature profiling, and vessel and mammal tracking, to name a few, demonstrate the marine potential of remotely sensed data. Air and space-borne sensors provide the best available means of monitoring huge tracts of ocean on a continuous and repetitive basis. The technological expertise already exists to support infrared sensing of the oceans; what is now required to advance the ocean imaging equation is tuning of algorithms, sensors, and measurement parameters along with further refinement of applications to support multiple data set integration. The authors provide an overview of the physics related to passive medium and long wave infrared imaging detectors. In addition, a process supporting selection of an infrared sensor for ocean based imaging is presented. From an operational perspective, the paper includes a comparison of medium-wave and long-wave images collected simultaneously using an airborne platform over coastal waters in eastern Newfoundland.

About the authors

Jordan Peckham is a doctoral candidate at Memorial University of Newfoundland. He holds a Master of Science in condensed matter physics where he studied light scattering from porous semiconductor materials. Currently, he is developing image processing algorithms for infrared sensors for deployment on unmanned aircraft. Dr. Siu O'Young is a professor with the Faculty of Engineering and Applied Science, Memorial University of Newfoundland. He conducts research on controls and unmanned aircraft systems focusing on the safe integration of unmanned aircraft for beyond line-of-sight missions. He is a contributing member of the RTCA SC-228 work group on defining detect and avoid standards for unmanned aircraft and is also an associate editor of *Journal of Unmanned Vehicle Systems*. Dr. John T. Jacobs is Senior Multi-Disciplinary Engineer at Raytheon Space and Aero Systems and serves as Raytheon technical liaison for university programs involving unmanned aerial vehicles, robotics, heat transfer, cybersecurity, image analysis algorithms, and ocean scarring.

COMPARISON OF MEDIUM AND LONG WAVE INFRARED IMAGING FOR OCEAN BASED SENSING

Jordan Peckham¹, Siu O'Young¹, and John T. Jacobs²

¹Faculty of Engineering and Applied Science, Memorial University of Newfoundland, St. John's, NL, Canada

²Raytheon, Goleta, CA, USA

ABSTRACT

Infrared thermal imagers convert the radiation received by a detector into a false colour visual image which represents the temperature profile of a scene or object. The selection of an infrared sensor for ocean based imaging is complicated, and depends on the intended use and target characteristics. This paper provides a theoretical understanding of the physics associated with the energy collected by the sensor and the resulting infrared images. Further, explanation of the factors affecting the resulting image with respect to the camera properties is provided. Finally, a variety of examples of airborne thermal images are presented, with detailed explanations of the imaged scenes based on theory and sensor characteristics provided in the previous sections.

INTRODUCTION

The infrared region of the electromagnetic spectrum refers to a wide range of wavelengths between 740 nm and 300 μm , much of which is not useful for ground or sea based imaging due to atmospheric absorption. The remaining transmitted bands are generally split into four categories as follows:

- Near Infrared (NIR) 0.75 - 1.4 μm ,
- Short-Wave Infrared (SWIR) 1.4 - 3 μm ,
- Medium-Wave Infrared (MWIR) 3 - 8 μm , and
- Long-Wave Infrared (LWIR) 8 - 15 μm [Pedrotti et al., 2007].

The medium wave and long wave infrared imaging systems can operate completely passive, with no external illumination required

since the imager senses the energy directly radiated from the object.

Medium wave infrared and long wave infrared sensors have been designed around two basic types of detectors. Medium wave infrared sensors typically use photon detectors, in which the radiation is absorbed within the material through interaction with electrons causing a change in the electronic energy distribution in the output. Long wave infrared sensors, on the other hand, employ thermal detectors, where the incident radiation is absorbed, which changes the temperature of the detector material [Rogalski, 2002]. Photon detectors boast many benefits over thermal detectors, including a lower signal to noise ratio, and a very fast response. However, in

general, photon detectors are heavier and more expensive, mainly due to cooling requirements of the semiconductor photodetectors. The slower and less-sensitive thermal detectors operate at room temperature and are much lighter and more rugged.

Currently, infrared imaging devices are being used in fields ranging from environmental monitoring, to building inspections, as well as medicine, agriculture, surveillance, and fire detection, to name a few. Airborne data collection is a large industry, with an increasing number of examples where infrared sensors are being deployed on manned and unmanned airborne platforms, including a number of aquatic and maritime applications. Using a long wave infrared camera, stream temperature measurements have been made using an unmanned aerial platform. Complex temperature profiles were reported, including warmer water in stagnant areas after corrections to the data for wind blowing across the imager's lens, and areas of high humidity [Jensen et al., 2012]. Coupling of infrared thermal imaging with an electro-optical imager allowed for determination of stream temperature measurements, previously unavailable to the extent and resolution that were measured, demonstrating the benefits of thermal imaging for environmental monitoring [Torgersen et al., 2001]. Long wave infrared imaging has also been demonstrated to solve some of the challenges associated with oil spill detection in water due to the uniform emissions in the long wave infrared band, and contrast of oil with surrounding water [FLIR, 2012]. Finally, use of infrared imagery for the detection and recognition of large vessels at sea has been

demonstrated, reporting an increased detection when compared to optical imaging technology [Withagen et al., 1999; Wu et al., 2011].

Several works have been published on the detection of large marine mammals, including observation of whales with temperatures 0.5-1.0°C warmer than surrounding sea temperatures, as well as blow temperature 0.3-4.0°C warmer than the surrounding water [Cuyler et al., 1992]. Tracking of the migration of grey whales over a three year period demonstrated that blows were visible both day and night, with a decreased probability of spotting blows on poor weather days [Perryman et al., 1999]. Further demonstration of the use of infrared imagery to detect whales based on spray patterns and body temperature was reported, noting the ineffectiveness of LWIR in high humidity conditions [Baldacci et al., 2005]. The first observations of a thermal footprint due to mixing of the stratified water resulting from the tail fluke of a whale was noted from a twin-engine airplane using LWIR imagery. This work reported that trails up to 300 m behind humpback whales, with an estimated average velocity of 2.4 m/s, were found. Under these conditions it was calculated that the thermal trail persisted for about two minutes [Churnside et al., 2009].

A comparison of MWIR and LWIR of a wake created by a ship revealed a dark wake pattern in the MWIR, and a bright pattern in the LWIR. This was attributed to strong surface reflection in the slick-like wake area. It was reported that for a ship moving at a steady rate, in the presence of surface heating which creates a temperature stratification in the top 10 metres of as much as 1°C, the wake

contrast will be significant [Voropayev et al., 2012]. An image processing algorithm to detect illegal sub-surface vessels based on the thermal wake scarring in the long wave infrared region was reported, with a low false detection rate, and the potential for real-time performance [Peckham et al., 2015].

This paper provides an overview of the physics related to infrared imaging devices, based mainly around passive detectors; MWIR and LWIR. Further, the process for the selection of an infrared sensor for ocean based imaging is presented, including a comparison of medium-wave and long-wave images collected simultaneously using an airborne platform over coastal waters in eastern Newfoundland.

THEORY

A thermal imager converts energy in the medium wave or long wave infrared region of the electromagnetic spectrum into a visual representation of the temperature profile of a scene. The total contributions of radiation of the thermal profile of a scene are a result of objects in the scene emitting radiation, as well as reacting to incident IR radiation by reflecting or absorbing some portion of it.

Measurement Process

Conservation of energy requires that the sum of the energy be equal to the incident energy, described with the coefficients of absorption, α , reflection, ρ , and transmission, τ , as [Pedrotti et al., 2007]

$$\alpha + \rho + \tau = 1. \quad (1)$$

A perfect blackbody is a perfect absorber of energy, such that $\alpha = 1$, and therefore $\rho = \tau = 0$.

Planck's Law describes the radiative properties of a perfect blackbody in terms of the spectral exitance, M_λ , as a function of temperature, T , and wavelength, λ , such that

$$M_\lambda(\lambda, T) = \frac{2\pi hc^2}{\lambda^5} \left(\frac{1}{e^{hc/\lambda k_B T} - 1} \right) \quad (2)$$

where h is Planck's constant, c is the speed of light, and k_B is Boltzmann's constant [Planck, 1901]. The wavelength of peak exitance, λ_{max} , determined by differentiating Equation 2 with respect to λ , (with $M_\lambda = 0$) is found to be

$$\lambda_{max} = \frac{hc}{5k_B T} = \frac{2897.885}{T} [\mu m \cdot K] \quad (3)$$

known as the Wien displacement law [Wien, 1896]. Further, the Stefan-Boltzmann law gives the total power emitted from a body, found by integrating Equation 2 over all wavelengths,

$$W = \sigma \cdot T^4 \quad (4)$$

where σ is the Stefan-Boltzmann constant [Stefan, 1879; Boltzmann, 1884]. Figure 1 presents Planck's Law for different temperature values between 273-1,000 K, along with calculated values for the wavelength of peak exitance and total radiant exitance corresponding to the curves. As the temperature increases, the wavelength of peak exitance decreases, while the total power emitted by the blackbody increases. At 273 K the value of peak exitance is 10.61 μm , whereas at 800 K the value of peak exitance is found to be 3.62 μm , which fall in the

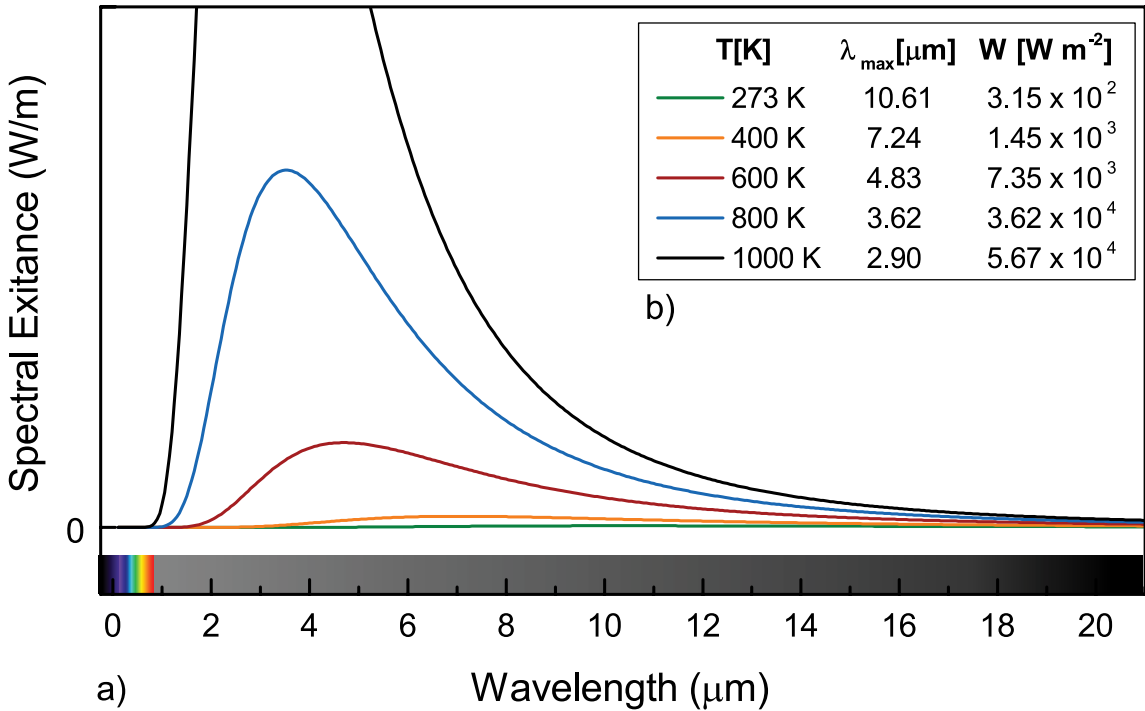


Figure 1: a) Illustration of Planck's Law at different temperatures. b) Calculated values of λ_{max} and W for each curve in a).

LWIR and MWIR range, respectively. Further, the total radiated energy at 800 K is found to be approximately 115 times larger than at 273 K.

To satisfy equilibrium conditions, Kirchoff's Law states that the coefficient of absorption must equal the emissivity, $\alpha = \varepsilon$, which describes the efficiency with which a blackbody radiates energy. Radiation from a real source is always less than a blackbody, however. In general, most materials studied for practical applications are assumed to be greybodies, which have a constant scale factor relative to a blackbody [Gade and Moeslund, 2014]. It follows then that for a real surface the emissivity can be defined as [Pedrotti et al., 2007]

$$\varepsilon = \frac{W_{obj}}{W} \quad (5)$$

where W_{obj} is the measured total radiant exitance from a surface, and w is the calculated total radiant exitance of a blackbody at the same temperature.

The radiation energy received by the sensor of an infrared camera is the sum of emitted radiation from the target object, the radiation from the surroundings reflected on the target object, and emitted radiation resulting from absorption of radiation in the atmosphere. It follows that the total radiation received by the sensor can be described as

$$M_{total} = \varepsilon \cdot \tau_{atm} \cdot M_{obj}(T_{obj}) + \rho \cdot \tau_{atm} \cdot M_{surr}(T_{surr}) + \varepsilon \cdot M_{atm}(T_{atm}) \quad (6)$$

where τ_{atm} accounts for attenuation in the atmosphere due to absorption and scattering

[Vollmer and Möllmann, 2010]. If the object is an opaque greybody, then $\tau=0$, and Equation 1 simplifies to give

$$\rho = 1 - \varepsilon \quad (7)$$

Further, it is reasonable to assume that atmospheric transmittance is dominated by absorption losses, such that $\varepsilon = 1 - \tau_{atm}$ [Pedrotti et al., 2007]. Therefore, Equation 6 becomes

$$M_{total} = \varepsilon \cdot \tau_{atm} \cdot M_{obj}(T_{obj}) + (1 - \varepsilon) \cdot \tau_{atm} \cdot M_{surr}(T_{surr}) + (1 - \tau_{atm}) \cdot M_{atm}(T_{atm}) \quad (8)$$

Atmospheric Effects

Atmospheric window regions are defined by molecular absorption by atmospheric molecules, primarily CO₂ and H₂O vapour. From Equation 8, it becomes obvious that thermal imaging is very sensitive to external influences on the radiation that the sensor detects [Vollmer and Möllmann, 2010]. The absorption of the radiated energy is related to the extinction coefficient, κ , as [Pedrotti et al., 2007]

$$\alpha(\lambda) = \frac{4\pi\kappa(\lambda)}{\lambda} \quad (9)$$

Figure 2 shows the atmospheric transmission of radiation from 0.9-5.6 μm and 7-26 μm in the skies above Mauna Kea Observatories in Hawaii (Data from Gemini Observatory [Lord, 1997]).

The absorption of a material also governs the penetration depth of the electromagnetic wave into a surface, such that according to the Beer-Lambert law, the intensity, I , decreases as

$$I(d) = I_o e^{-\alpha \cdot d} \quad (10)$$

where I_o is the initial intensity, and d is the depth. The penetration depth, δ_p , is simply $\alpha = \delta_p^{-1}$ [Hecht, 2001]. The absorption coefficient, α , holds much different quantities depending on the wavelength (see Figure 3). In the visible region of the electromagnetic spectrum (390 nm-750 nm) the absorption reaches below 0.001 cm⁻¹ with penetration depths to almost 1,000 m. In this region the transmittance is much larger than zero, as expected as water is a transparent material. Conversely, in the infrared wavelength range (770 nm-100 μm) water is essentially opaque,

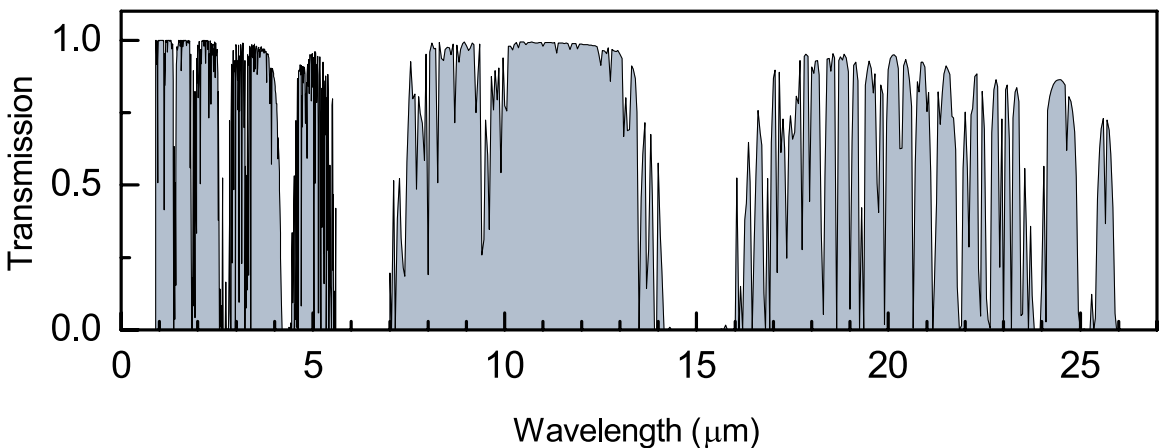


Figure 2: Atmospheric transmission plotted for 0.9-5.6 μm and 7-26 μm . Data collected at the Mauna Kea Observatories, generated using the ATRAN modelling software [Lord, 1992] and provided by the Gemini Observatory [Lord, 1997].

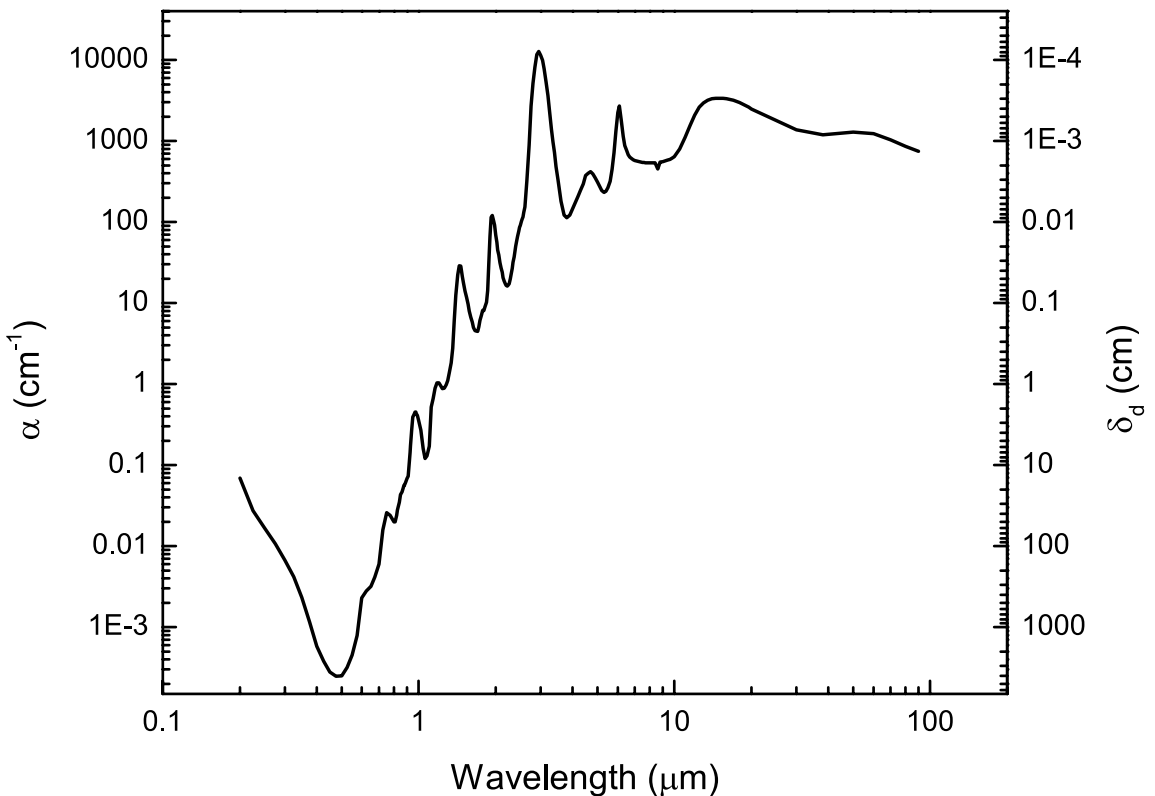


Figure 3: Absorption coefficient and penetration depth from 200 nm to 100 μm of water at 298 K [Hale and Querry, 1973].

with a transmittance of approximately zero. Absorption coefficient values are between 0.1 and 10^4 cm^{-1} , such that infrared radiation is absorbed between 10 μm and 1 m of the water's surface [Hale and Querry, 1973].

IR SENSOR SELECTION PARAMETERS

An understanding of the parameters which affect the resulting data collected by an infrared camera is required to maximize its use for detection, tracking or other applications.

Spectral Band

The two wavelength windows of importance for thermal imaging are medium wave infrared and long wave infrared. The 5-8 μm range is unusable due to absorption by water vapour in the atmosphere (note that $\tau=0$ in this range in Figure 2). Depending on the application, the

wavelength range of the sensor has a significant impact on the results. Moreover, LWIR and MWIR differ with respect to atmospheric transmission. MWIR has superior clear weather performance, with a higher transmissivity under high humidity, whereas LWIR performs better in fog and dust conditions, and has a higher tolerance to atmospheric turbulence [Dakin and Brown, 2010]. By comparison, in a category II fog, in which the visual detection range is 0.61 km, it has been reported that the detection range was 0.54 km and 2.4 km for MWIR and LWIR, respectively [FLIR, 2013].

Thermal Resolution

The thermal resolution of an infrared imager is the smallest temperature difference that can be measured by the sensor. This measure is commonly expressed as the NETD, or noise

equivalent temperature difference, determined as the temperature difference which produces a signal equal to the sensor's temporal noise [FLIR, 2014]. NETD is determined by multiplying the detector's RMS noise by the signal measured over the temperature difference. Currently available uncooled LWIR sensors report a NETD of approximately 30 mK. Cryogenically cooled detectors have an increased sensitivity, resulting in a lower NETD value, with currently available cryogenically cooled MWIR and LWIR reporting NETD values less than 20 mK and 25 mK, respectively. Cryogenic cooling becomes a requirement when an increased sensitivity is needed in the wavelength range of the imager [FLIR, 2013].

Integration Time

The exposure time represents the time required for an infrared sensor to capture a single frame of data, commonly also referred to as the exposure time or thermal time constant. It is analogous to the shutter speed of a digital camera, where the opening and closing of the shutter to collect the photons creates a single frame. If an infrared camera is moving quickly, a shorter exposure time is desired since it is

less likely to result in image blurring. However, the shorter integration time may result in under-exposure. Longer exposure times allow more collection of the incoming energy from an object, but will result in blurring for a quickly moving frame. In general, there is an inverse relationship between exposure time and sensor sensitivity, where highly sensitive sensors require less time to collect the same image. Moreover, the integration time also affects the frame rate that the infrared imager can record data. With frame rates ranging from 9 Hz up to 380 Hz, a higher frame rate increases the amount of data collected.

Field of View

The field of view (FOV) is the angular extent of the observable target field, defined by the lens and detector area of the imager [Vollmer and Möllmann, 2010]. The field of view can be calculated as

$$FOV = 2 \cdot d \tan \frac{\theta}{2} \quad (11)$$

where d is the distance to the scene, and θ is the angle of view. Figure 4 shows the field of view for an imager where hFOV is the

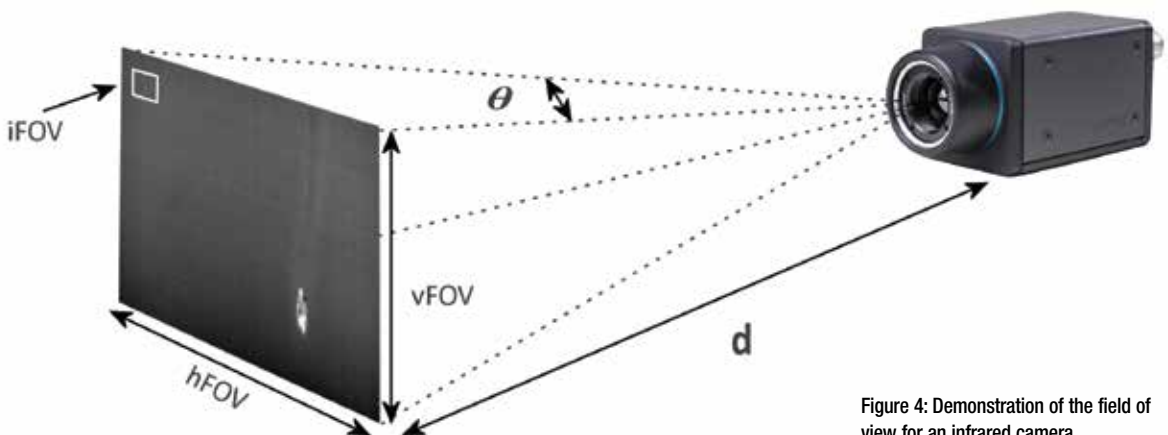


Figure 4: Demonstration of the field of view for an infrared camera.

Device	IR Range	Detector	Resolution	NETD	Integration Time	Frame Rate
FLIR Photon640	7.5 - 13.5 μm	Vanadium Oxide	644 x 512	50 mK	10 ms	9 Hz
FLIR SC5000	2.5 - 5.1 μm	Indium Antimonide	640 x 512	20 mK	1 μs - 20 ms	60 Hz

Table 1: Infrared imager specification comparison for cameras used during the data collection presented.

horizontal field of view, vFOV is the vertical field of view, and iFOV is the instantaneous field of view. The spatial resolution of the focal plane array describes the instantaneous field of view. This is the extent of an individual pixel, determined by dividing the FOV by the pixel dimension of the given axis.

The iFOV can be increased by decreasing the distance between the imager and target, or by decreasing the angle of view of the infrared camera. For example, if an infrared imaging device is fixed to an aircraft flying at an altitude of 150 m above sea level, where the lens of the imager has an angle of view of $26^\circ \times 20^\circ$, the FOV is determined to be 69.3 m x 52.9 m, and the iFOV is calculated to be 10.8 cm/pixel x 10.3 cm/pixel. If θ remains constant, and d is increased to 600 m above sea level, the FOV becomes 277.0 m x 211.6 m, and the iFOV is 43.0 cm/pixel x 41.3 cm/pixel. If instead the angle of view of the IR camera is $14^\circ \times 11^\circ$, the FOV at 600 m would be 147.3 m x 115.5 m, and the iFOV would be 22.9 cm/pixel x 22.6 cm/pixel. If the object of interest is known, selecting a lens such that the object fills the FOV will result in the best imagery with the most measurement data on the object.

Bit Depth

The total number of intensity values that can be stored for a given scene is dependent on

the bit-depth of the recorded data. In general, infrared images are recorded as 8-bit or 14-bit images, and with 2^n available bins, this results in 256 and 16,384 individual intensity bins available for the recorded data, respectively. If the NETD of the imager is 50 mK, the range of temperature values available for a 8-bit imager is 12.8 K, whereas for a 14-bit imager is 814.2 K.

RESULTS AND DISCUSSION

Experimental Design

The data presented in this section were collected from a float plane in the channel between Portugal Cove and Bell Island in Newfoundland, Canada. The approximate average speed of the aircraft was 60 knots, with a height above sea level between 150 m and 300 m. On the day the data was collected, St. John's International Airport reported a mean temperature of 12°C , with a maximum temperature of 15.3°C , and a minimum temperature of 8.6°C . A FLIR Photon 640 LWIR camera, a FLIR SC5000 MWIR camera, and a Panasonic video recorder were mounted on a hand-held platform, with approximately 20 cm between each camera. Table 1 presents a comparison of the specifications of the thermal imaging devices used. It should be noted that the intensity values of the medium wave infrared images have been adjusted using *imadjust* in MATLAB [2012] so the 14-bit data could be viewed.

Infrared Image Comparison

Figure 5 shows a comparison of an optical, medium wave infrared, and long wave infrared image taken from an aerial platform of a 52 m x 15 m ship, travelling with an average speed of 10.2 knots. In both the MWIR and LWIR images, the ship appears lighter than the surrounding water, indicating that the ship temperature is higher. Calculating λ_{max} assuming that the temperature of the water is approximately 5°C and the temperature of the ship is 12°C, Equation 3 gives 10.4 μm and 10.2 μm , respectively. The wavelength of maximum exitance for both the ship and the surrounding ocean falls within the LWIR region, indicating that the majority of the radiation in the scene falls in this thermal band as well.

For military and surveillance uses, it is generally accepted that MWIR imaging yields the best results for imaging and detection of vehicles, ships, and aircraft due to the increased sensitivity to these objects [Rogalski, 2002]. The emissivity values for water and steel are 0.96 and 0.16, respectively [Gubareff et al., 1960]. By combining Equation 4 and Equation 5, an equation for the total radiant exitance for a greybody is found, $W_{obj} = \epsilon \cdot \sigma \cdot T^4$. Therefore, the total peak exitance for the surrounding ocean water and the ship is found to be 325 W/m² and 60 W/m², respectively. Based on this calculation the surrounding water could easily be assumed to dominate the energy received by the sensor. However, according to Equation 7, an object with a low emissivity value has a high coefficient of reflectance. Recall from Equation 8 that an infrared imager does not receive the temperature of an object, but

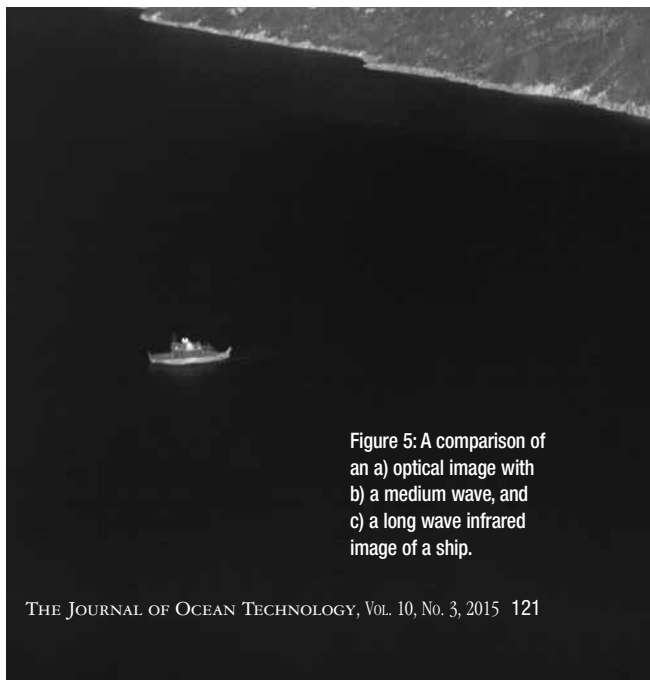


Figure 5: A comparison of an a) optical image with b) a medium wave, and c) a long wave infrared image of a ship.

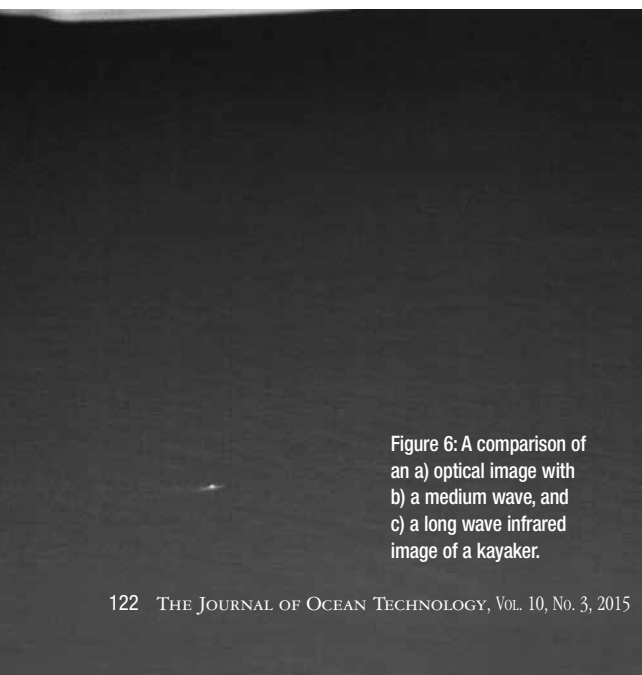
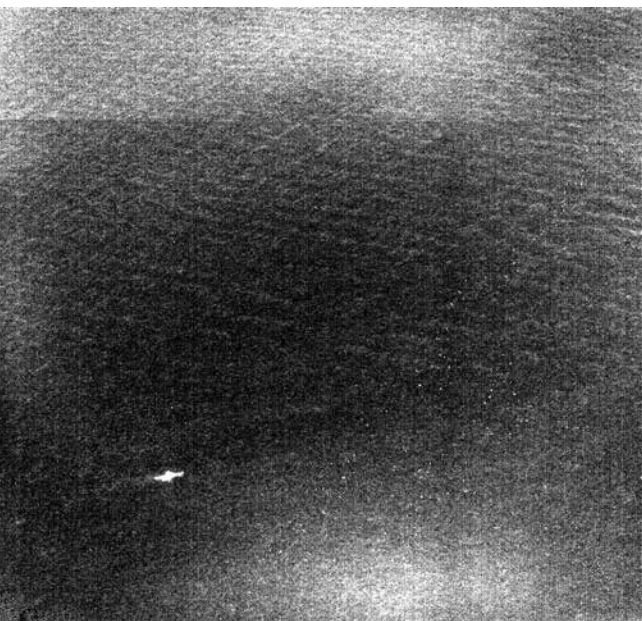


Figure 6: A comparison of an a) optical image with b) a medium wave, and c) a long wave infrared image of a kayaker.

instead the energy of the scene. For example, a steel sheet with a piece of plastic tape ($\epsilon = 0.95$) fixed to it have the same measured temperature. If the steel and the plastic are warmed to a higher temperature than the surroundings, the plastic will appear much brighter in the infrared image than the steel. Conversely, if the set is cooled below the temperature of the surroundings, the plastic will appear much darker than the steel. Despite the temperature of both the plastic and the steel being equal, since the emissivity of the plastic is higher, meaning it is an efficient emitter, while the emissivity of the steel is low. As such, the plastic will more closely indicate the actual temperature of the surface. The radiation received from the steel is a better indicator of the background temperature since the steel is reflecting the background radiation. Therefore, since the surrounding water in Figure 5 has a higher emissivity value than the ship, and the surroundings are warmer than the water, then the water represents the target temperature better than the ship. Further, the steel ship gives a better indication of the background temperature due to its high reflectivity value.

This idea is further demonstrated in Figure 6 which shows a comparison of visible, MWIR and LWIR images of a fibreglass kayak in the ocean. It would be expected that the kayak would be approximately the same temperature as the air-water interface. However, the kayak, with approximate emissivity of 0.75, is much more prominent than the background. Emissivity is not a simple material property, however, especially since factors such as the shape and viewing angle can affect the emissivity of the object.

Figure 7 presents a set of images of a small boat travelling through the scene. Comparing the medium wave and long wave infrared images, Figures 7b and 7c, respectively, with the corresponding optical image, the wave patterns seen in the optical image are still found in the medium wave infrared image but not in the LWIR image. Blurring of the image in the long wave infrared image due to a longer integration time is the cause of the reduced sharpness. If we assume that the aircraft speed is 60 knots, and the integration time for a single frame for the FLIR Photon 640 is approximately 10 ms, then during the collection of radiation for a single image, the aircraft moves slightly over 30 cm. For comparison, if the FLIR SC5000 has an integration time of 10 μ s, then the aircraft movement during the imaging process is approximately 3 mm. If the height above sea level of the infrared imager is 150 m, with a FOV of 26° x 20°, the iFOV is 10.8 cm/pixel x 10.3 cm/pixel. So for each frame of the recorded infrared image for the Photon 640, each pixel in the image would represent an average of a ground area equal to approximately 10 cm x 40 cm. If the altitude is increased to 600 m above sea level, the iFOV becomes 58.6 cm/pixel x 43.0 cm/pixel, and the ocean area averaged during a single frame is larger than 0.3 m².

Reflection of sunlight from the ocean surface creates problems in image processing for detection and tracking applications of both optical and infrared images. Figure 8 presents an image set where a small boat is travelling directly through the reflected sunlight. In both the optical and medium wave infrared images, Figure 8a and 8b, the sun's reflection saturates

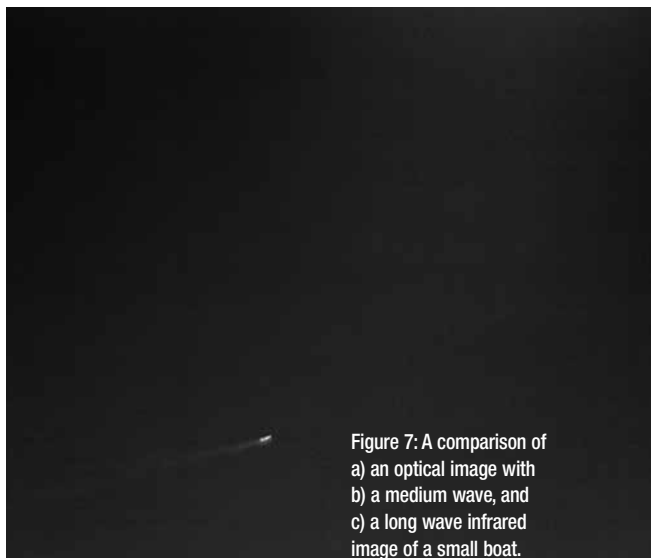


Figure 7: A comparison of a) an optical image with b) a medium wave, and c) a long wave infrared image of a small boat.

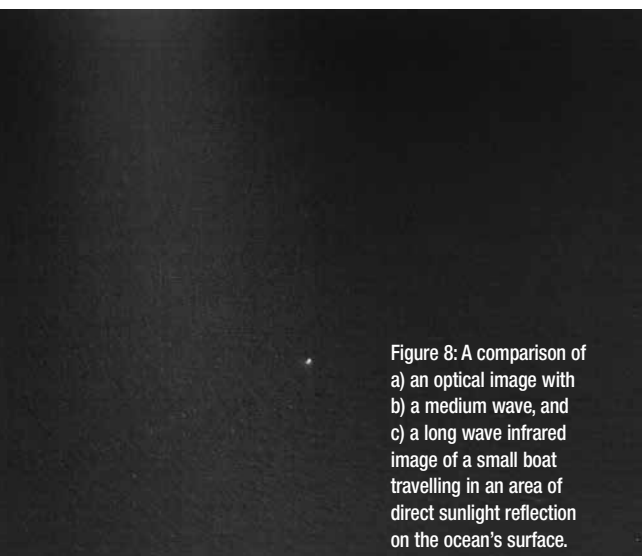


Figure 8: A comparison of a) an optical image with b) a medium wave, and c) a long wave infrared image of a small boat travelling in an area of direct sunlight reflection on the ocean's surface.

approximately half of the imaged scene. In particular, the target in the MWIR image is much less visible than previously seen. However, in the LWIR image, Figure 8c, the sun's reflection is not apparent in the image, with the target to background contrast being quite good. Solar interference is noted as a problem in the visible band and medium wave infrared images [FLIR, 2012]. In the long wave infrared band, solar rays are diffusely reflected from the water surface. In fact, one of the major advantages of LWIR sensors for target detection and tracking is the uniform signal in most conditions, both day and night [FLIR, 2013].

Reflections from objects have a significant effect on the appearance of a thermal profile [Dakin and Brown, 2010]. It was demonstrated that for a 17°C object, the received radiation in the MWIR band was 24 W/m² from reflected solar radiation, and 4.1 W/m² from the emission of the blackbody. Conversely, in the LWIR thermal band for the same object, the reflected solar radiation at ground level was 1.5 W/m², whereas the emitted radiation was 127 W/m². Reflected sunlight is nearly negligible in the LWIR band, whereas in the MWIR band it dominated the received signal [Burnay et al., 1988]. However, the thermal contrast of this scene, arising from temperature variations and differences in emissivity, will be larger in the MWIR image [Dakin and Brown, 2010]. This concept is further demonstrated in Figure 9. In the medium wave infrared image, the pavement, $\epsilon = 0.90-0.98$, has a very high contrast when compared to the surrounding trees and grass, whereas in the long wave infrared image the contrast is not as large.

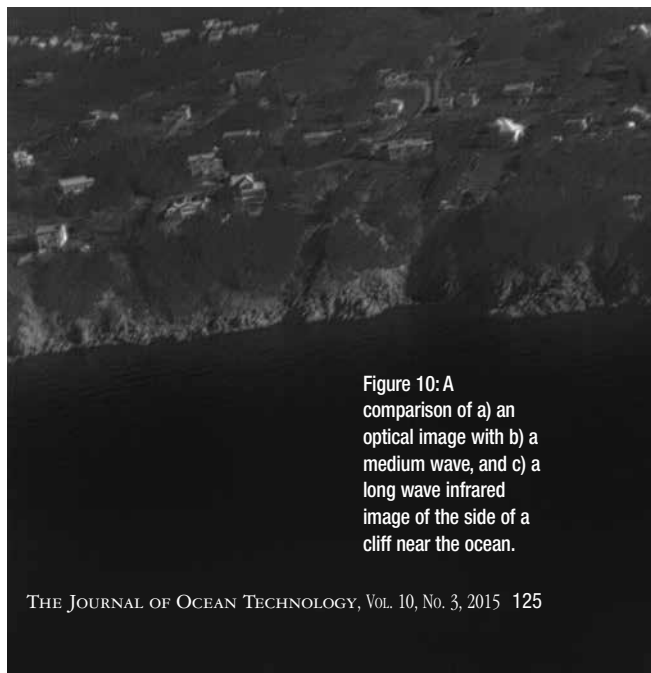


Figure 9: A comparison of a) an optical image with b) a medium wave, and c) a long wave infrared image of a highway.

Figure 10: A comparison of a) an optical image with b) a medium wave, and c) a long wave infrared image of the side of a cliff near the ocean.

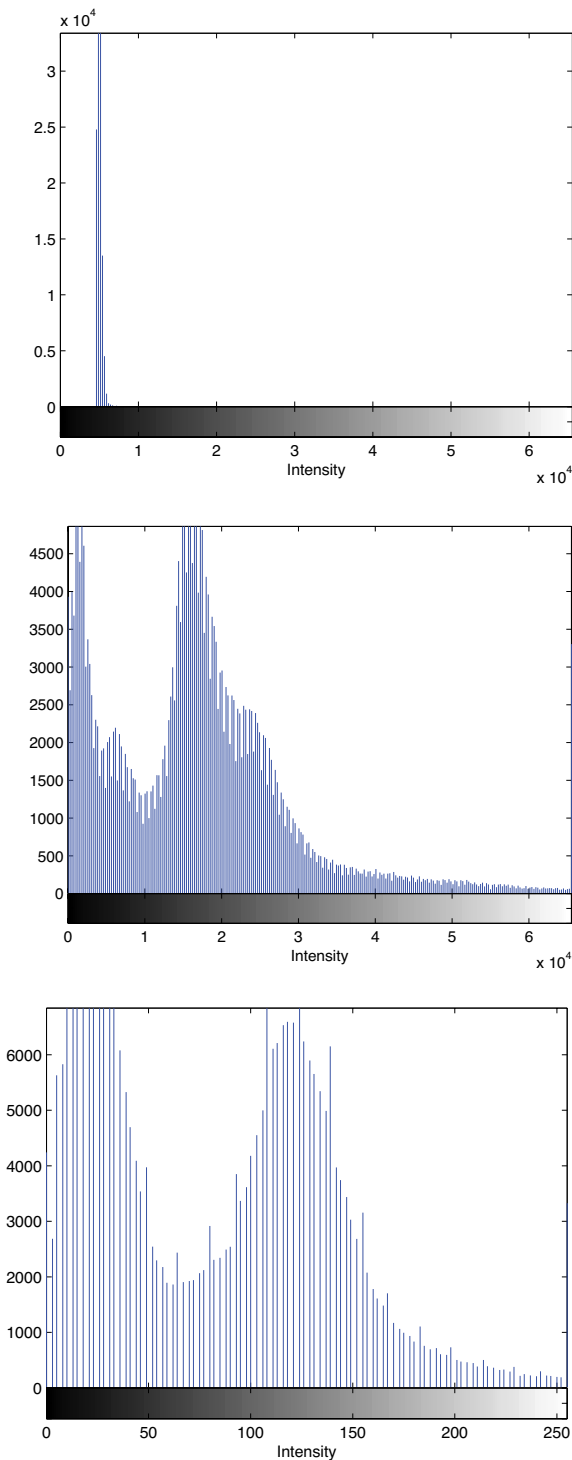


Figure 11: A comparison of the histograms of the a) medium wave, b) the adjusted medium wave, and c) the long wave infrared images presented in Figure 10.

Figure 10 shows an image of a cliff near the edge of the ocean. This is a more complex scene than has been presented in the previous images with respect to the wider temperature range. With distinct levels in the range of $[0, 16,383]$ for a 14-bit image, the number of discrete bins can be much larger than an 8-bit image format. Figure 11 presents the histograms of the thermal images in Figure 10. The histogram in Figure 11a is the original histogram of Figure 10b before adjustment. The intensity values range from 4,706 to 7,935, with all 3,229 bins filled. From Table 1, the NETD of the SC5000 is 20 mK, which gives an approximate temperature range in the scene of 64.6°C . The large temperature range in this image is due to higher apparent temperatures of objects in the scene. It should be noted that for the histograms presented here, the range of the x-axis is $[0, 65,535]$, which corresponds to a 16-bit image, due to image storage standards. The range of intensity values is better seen in Figure 11b. The corresponding histogram for the long wave IR image is given in Figure 11c. In this case, each of the 255 bins are filled.

CONCLUSIONS

A review of the background of infrared thermal remote sensing was presented. The physical relationship between theoretical blackbodies and real surfaces was described, aiding in the interpretation of the emission of radiant energy from objects in the thermal scenes. Using a radiometric chain technique, an equation (Equation 8) for the infrared radiation of a real scene was derived. Thermal infrared imaging devices and the factors which effect the resulting image quality were

discussed, with particular reference to the physics of the detectors, platforms, and scenes. Comparisons of sample visible, MWIR and LWIR images were presented, with discussion of the differences arising due to the characteristics of the sensors and the thermodynamics of the scenes.

REFERENCES

- Baldacci, A.; Carron, M.; and Portunato, N. [2005]. *Infrared detection of marine mammals*. NATO Undersea Research Center, Technical Report.
- Boltzmann, L. [1884]. *Derivation of Stefan's law concerning the dependence of the thermal radiation on the temperature of the electro-magnetic theory of light*. *Annalen der Physik und Chemie*, Vol. 22, pp. 291-294.
- Burnay, S.; Williams, T.; and Jones, C. [1988]. *Applications of thermal imaging*. Taylor Francis.
- Churnside, J.; Osrovsky, L.; and Veenstra, T. [2009]. *Thermal footprint of whales*. *Oceanography*, Vol. 22, pp. 206-209.
- Cuyler, L.C.; Wiulsrod, R.; and Oritsland, N.A. [1992]. *Thermal infrared radiation from free living whales*. *Marine Mammal Science*, Vol. 8, p. 120.
- Dakin, J. and Brown, R. [2010]. *Handbook of optoelectronics* (two-volume set). Taylor Francis.
- FLIR [2012]. *Oil spill detection with infrared imaging*. Technical Report. Retrieved from: http://www.flir.com/uploadedFiles/CVS_Americas/Maritime_-_NEW/Case_Studies/FLIR-Oil-Spill-Application-Note.pdf.
- FLIR [2013]. *Seeing through fog and rain with a thermal imaging camera*. Technical Report. Retrieved from: http://www.flirmedia.com/MMC/CVS/Tech_Notes/TN_0001_EN.pdf.
- FLIR [2014]. *The ultimate infrared handbook for research and development professionals*. Technical Report. Retrieved from: <http://www.flir.com/science/display/?id=69528>.
- Gade, R. and Moeslund, T.B. [2014]. *Thermal cameras and applications: a survey*. *Machine Vision and Applications*, Vol. 25, pp. 245-262.
- Gubareff, G.; Janssen, J.; and Torborg, R. [1960]. *Thermal radiation properties survey: a review of the literature*. Honeywell Research Center.
- Hale, G.M. and Querry, M.R. [1973]. *Optical constants of water in the 200-nm to 200-m wavelength region*. *Applied Optics*, Vol. 12, pp. 555-563.
- Hecht, E. [2001]. *Optics*, 4th edition. Addison Wesley.
- Jensen, A.; Neilson, B.; McKee, M.; and Chen, Y. [2012]. *Thermal remote sensing with an autonomous unmanned aerial remote sensing platform for surface stream temperatures*. *Geoscience and Remote Sensing Symposium, IEEE International*, July, pp. 5049-5052.
- Lord, S.D. [1992]. *A new software tool for computing Earth's atmospheric transmission of near- and far-infrared radiation*. Technical Report, December.
- Lord, S.D. [1997]. *NASA technical memorandum 103957*. Gemini Observatory, Technical Report.
- MATLAB [2012]. *Version 7.14.0739 (R2012a)*. Natick, Massachusetts: The MathWorks Inc.
- Peckham, J.; Shehata, M.; O'Young, S.; and Jacobs, J.T. [2015] *Development of an*

- algorithm to detect sub-surface vessels using infrared imagery*. Submitted to Geoscience and Remote Sensing Letters.
- Pedrotti, F.; Pedrotti, L.; and Pedrotti, L. [2007]. *Introduction to optics*. Pearson Prentice Hall.
- Perryman, W.L.; Donahue, M.A.; Laake, J.L.; and Martin T.E. [1999]. *Diel variation in migration rates of eastern pacific gray whales measured with thermal imaging sensors*. Marine Mammal Science, Vol. 15, p. 426.
- Planck, M. [1901]. *On the law of distribution of energy in the normal spectrum*. Annalen der Physik, Vol. 4, p. 553.
- Rogalski, A. [2002]. *Infrared detectors: an overview*. Infrared Physics and Technology, Vol. 43, p. 187.
- Stefan, J. [1879]. *About the relationship of heat radiation and temperature*. Sitzungsberichte der Kaiserlichen Akademie der Wissenschaften, Vol. 79, pp. 391-428.
- Torgersen, C.E.; Faux, R.N.; McIntosh, B.A.; Poage, N.J.; and Norton, D.J. [2001]. *Airborne thermal remote sensing for water temperature assessment in rivers and streams*. Remote Sensing of Environment, Vol. 76, p. 386.
- Vollmer, M. and Möllmann, K. [2010]. *Infrared thermal imaging: fundamentals, research and applications*. Wiley.
- Voropayev, S.I.; Nath, C.; and Fernando, H.J.S. [2012]. *Thermal surface signature of ship propeller wakes in stratified waters*. Physics of Fluids, Vol. 24, p. 116603.
- Wien, W. [1896]. *Concerning the energy distribution in the emission spectrum of a blackbody*. Annalen der Physik, Vol. 294, No. 8.
- Withagen, P.; Schutte, K.; Vossepoel, A.; and Breuers, M. [1999]. *Automatic classification of ships from infrared (FLIR) images*. In: Signal Processing, Sensor Fusion, and Target Recognition VIII, Proceedings of the Society of Photo-Optical Instrumentation Engineers. I. Kadar (Ed.), Vol. 3720, pp. 180-187.
- Wu, J.; Mao, S.; Wang, X.; and Zhang, T. [2011]. *Ship target detection and tracking in cluttered infrared imagery*. Optical Engineering, Vol. 50, No. 5.